

Ultrafast graphene photodetector

Fengnian Xia^{†*}, Thomas Mueller[†], Yu-ming Lin, Alberto Valdes-Garcia and Phaedon Avouris^{*}

Graphene research so far has focused on electronic^{1–6} rather than photonic applications, in spite of its impressive optical properties^{7,8}. These include its ability to absorb ~2% of incident light over a broad wavelength range despite being just one atom thick⁷. Here, we demonstrate ultrafast transistor-based photodetectors made from single- and few-layer graphene. The photoresponse does not degrade for optical intensity modulations up to 40 GHz, and further analysis suggests that the intrinsic bandwidth may exceed 500 GHz. The generation and transport of photocarriers in graphene differ fundamentally from those in photodetectors made from conventional semiconductors as a result of the unique photonic and electronic properties of the graphene. This leads to a remarkably high bandwidth, zero source-drain bias and dark current operation, and good internal quantum efficiency.

Graphene is a single-atomic-layer, two-dimensional system composed solely of carbon atoms arranged in a hexagonal honeycomb lattice. It has a linear energy dispersion relation, implying a vanishing effective mass, a high Fermi velocity (~1/300 of the speed of light), and a huge electrical mobility approaching 200,000 cm² V⁻¹ s⁻¹ for a free sheet for both electrons and holes^{1–5}. Moreover, the photonic properties of graphene are equally remarkable: despite being only a single atomic layer thick, it can absorb photons at least from the visible to the infrared range, and the strength of the interband transition in graphene is one of the largest of all known materials^{7,8}. By comparison, ultrathin (less than a few nanometres) III–V quantum wells can be transparent to a broad range of infrared light due to the blueshift of the absorption edge induced by energy quantization⁹. Multiple graphene layers absorb additively, and the absorption range of the system can be tuned by changing the Fermi energy using an external gate field^{8,10}.

The combination of the exceptional transport and optical properties of graphene suggests novel photonic devices fundamentally different from conventional arrangements. It has been proposed previously that graphene nanoribbons with a bandgap could be used as phototransistors¹¹. Here, we explore the use of zero-bandgap, large-area single or few-layers of graphene field-effect transistors (FETs) as ultrafast photodetectors. On light absorption, the generated electron–hole pairs in graphene would normally recombine on a timescale of tens of picoseconds, depending on the quality and carrier concentration of the graphene^{12–14}. If an external field is applied, the pairs can be separated and a photocurrent is generated. The same happens in the presence of an internal field. Such fields have been shown to be formed near the metal electrode–graphene interfaces^{15–17}. Here, we demonstrate that these internal fields can be used to produce an ultrafast photocurrent response in graphene. Owing to the high carrier transport velocity existing even under a moderate *E*-field, no direct bias voltage between source and drain (photocurrent generation path) is needed to ensure ultrafast and efficient (6–16% internal quantum efficiency within the photodetection region) photocurrent generation. Such a zero-bias operation has been demonstrated previously

in special unitravelling-carrier photodiodes (UTC-PD) with much higher built-in *E*-field for high-bandwidth operation^{18,19}. However, in most conventional photodiodes, large external bias directly applied to the photodetecting area and its complete depletion are essential for fast and efficient photodetection²⁰. Graphene photodetectors may find a wide range of photonic applications including high-speed optical communications, interconnects, terahertz detection, imaging, remote sensing, surveillance and spectroscopy^{20–24}.

Figure 1a shows a scanning electron microscopy (SEM) image of the graphene devices. The optical microscope image in the inset shows the same graphene devices at lower magnification. The number of graphene layers is first estimated from the colour of the optical images and then confirmed by Raman spectroscopy²⁵. The SiO₂ film underneath the graphene is 300 nm thick, and the substrate is highly resistive silicon (1–10 kΩ cm), to minimize the parasitic capacitance. Two types of high-frequency coplanar waveguide wirings are shown: ground–signal (G–S) and ground–signal–ground (G–S–G)²⁶. The results presented in the main text are obtained from a device with two to three layers of graphene in the G–S wiring scheme. Results from single-layer graphene are presented in the Supplementary Information. The fabrication and layout of the devices are discussed in the Methods section.

A high-frequency electrical model of the graphene device is shown in Fig. 1b. It can be modelled by the pad capacitance (*C_p*) in parallel with the graphene capacitance (*C_g*) and graphene resistance (*R_g*), as shown by the green symbols from top to bottom in Fig. 1b. The graphene capacitance *C_g* quantifies the correlation between the total channel charge and the source–drain bias. The total high-frequency impedance *Z_{IN}* is given by

$$Z_{\text{IN}} = \frac{R_g}{1 + j2\pi f R_g (C_p + C_g)} \quad (1)$$

where *f* is the frequency of the excitation electric signal. The impedance can be determined from the measured high-frequency reflection coefficient *Γ_{IN}*, from which the resistive and capacitive components may be inferred²⁷. Details regarding the high-frequency calibration and measurement are presented in the Methods section. The measured total capacitance (*C_p* + *C_g*) and *R_g* in the high-frequency domain are plotted in Fig. 1c as a function of the gate bias. Also shown in Fig. 1c is the d.c. resistance measured between the source and drain of the same graphene device. The graphene resistance measured using the reflection approach in the high-frequency domain describes the gate dependence well with a maximum deviation of ~15% from the corresponding d.c. measurements. Separate measurements on naked G–S contact pads reveal a gate-bias-insensitive *C_p* value ranging from 20 to 25 fF, indicating that the graphene capacitance *C_g* strongly depends on the gate bias and therefore channel Fermi level²⁸.

Photocurrent generation experiments were performed at both low (100 Hz or d.c.) and high (10 MHz to 40 GHz) light intensity

IBM Thomas J. Watson Research Centre, Yorktown Heights, New York 10598, USA; [†]These authors contributed equally to this work.

*e-mail: fxia@us.ibm.com; avouris@us.ibm.com

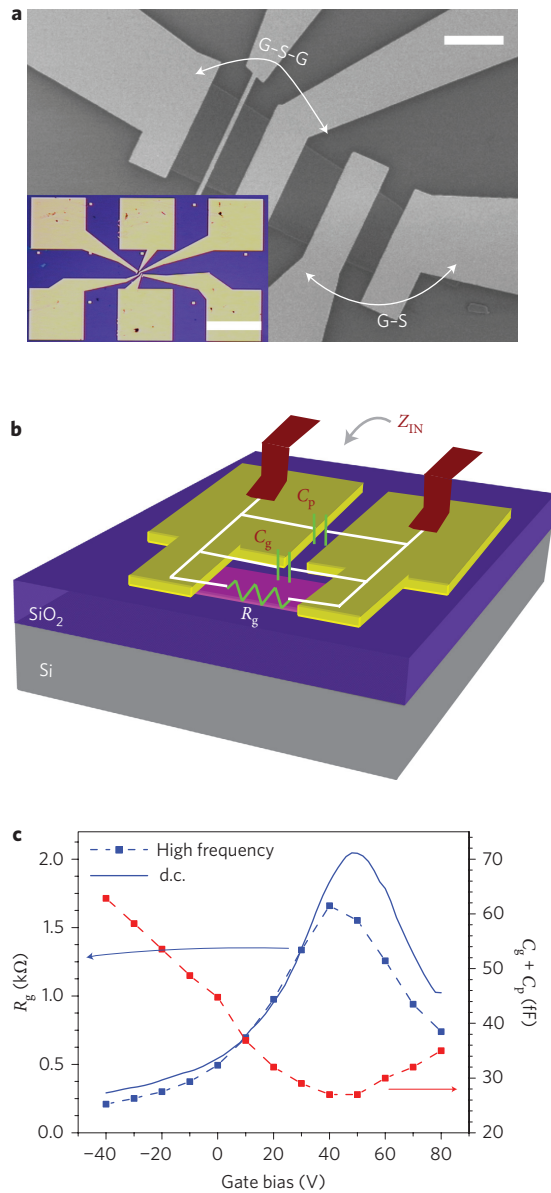


Figure 1 | Electrical characterizations of the graphene photodetector.

a, SEM and optical (inset) images of the high-bandwidth graphene photodetectors. The graphene shown here has two to three layers. Two types of wirings are shown: ground-signal (G-S) and ground-signal-ground (G-S-G). The high-frequency results are from devices with G-S wirings. Scale bars: main panel, 2 μm ; inset, 80 μm . **b**, Device schematics and electrical model in the high-frequency domain. The high-frequency reflection coefficient Γ_{IN} is measured using a network analyser, and Z_{IN} is inferred from Γ_{IN} . The green symbols, from top to bottom, represent C_{p} , C_{g} and R_{g} , respectively. The purple sheet represents the graphene, and a pair of dark red strips denote the microwave probe tips. **c**, Measured circuit parameters in d.c. and high-frequency domains at different gate biases. Solid blue, d.c. resistance; blue and red dots, resistance and total capacitance in the high-frequency domain from reflection measurements.

modulation frequencies. Figure 2a shows typical d.c. current measurements as a function of the source-drain bias with and without light illumination at a fixed gate bias. The dark current is represented by the dashed line, which extrapolates through the origin. In this work, the photocurrent is always studied at or close to a short-circuit condition. The magnitude of the photocurrent strongly depends on the location of the optical illumination and

also on the gate bias as reported previously¹⁶. Photocurrent imaging experiments at a lock-in frequency of 100 Hz were therefore carried out to determine the optimal illumination locations at various gate biases¹⁶. Usually, the strongest photocurrent is observed when light is incident near the metal-graphene interfaces where the strongest E -fields form in our p-type FETs. However, at a large positive gate bias, the middle of the channel turns n-type, and the graphene in the vicinity of the metal remains p-type due to metal-induced doping. Thus, graphene p-n junctions are formed on both sides of the device and the maximum E -field moves towards the centre of the channel for up to 0.5 μm (refs 16,17). The peak d.c. photoresponsivity⁹ $R_{\text{d.c.}}$, defined as $I_{\text{ph}}/P_{\text{opt}}$, where I_{ph} is the photocurrent and P_{opt} the total incident optical power on the graphene, as a function of gate bias, is shown by the red dots in the inset of Fig. 2b. A maximum external d.c. photoresponsivity of $\sim 0.5 \text{ mA W}^{-1}$ is achieved at a gate bias of 80 V. The estimated internal quantum efficiency within the high E -field photodetection region is in the range 6–16%. Moreover, the external photoresponsivity can be enhanced by enhancing the interaction between the light and graphene²¹. A detailed discussion on the efficiency is presented in the Supplementary Information.

Following the low-frequency measurement of the photocurrent, we performed high-frequency photoresponse measurements from 10 MHz to 40 GHz using a commercial light-wave component analyser, which measures the peak a.c. photoresponsivity as a function of the light intensity modulation frequency. Detailed information about the measurements can be found in the Methods. Figure 2b shows the relative a.c. photoresponse of the graphene device, $S_{21}(f)$, as a function of the light modulation frequency f up to 40 GHz at a gate bias of 80 V. Here, $S_{21} = 20 \times \log_{10}(R_{\text{a.c.}})$ (amp/watt)/1 (amp/watt) and $R_{\text{a.c.}}$ is the a.c. photoresponsivity defined as $\Delta I_{\text{ph}}/\Delta P_{\text{opt}}$, where ΔI_{ph} and ΔP_{opt} are the variation of the photocurrent and incident optical power, respectively. The curve is intentionally displaced vertically so that the response starts at 0 dB. No photoresponse degradation from the graphene device was observed up to our measurement limit of 40 GHz. The ~ 1 dB response degradation seen in Fig. 2b was not introduced by the graphene device, but rather by the microwave probes as specified by the manufacturer. The absolute a.c. photoresponsivity of the same graphene device was measured using a different setup with maximum operational frequency up to 26 GHz. This setup has lower noise, so it allows for the accurate measurement of a.c. photoresponsivity at all gate biases. A number of frequency response curves were measured and are plotted in Fig. 2c; no measurable photoresponse degradation was observed at any gate bias. The amplitude of the high-frequency photoresponse does show strong gate dependence, which is similar to that in d.c. measurements. We plotted the high-frequency a.c. photoresponsivity $R_{\text{a.c.}}$ as the blue dots in the inset of Fig. 2b, resulting in a curve almost identical to the d.c. one, further supporting the high-bandwidth nature of the photoresponse.

The mechanism for the generation and collection of the photo-carriers is shown schematically in Fig. 3a,b. When light is incident in the high E -field region, electron-hole pairs are generated and separated. In the open-circuit case, these photogenerated carriers are separated by internal fields, but do not produce a current in external circuits. Instead, an open-circuit voltage V_{OC} is produced across the carrier generation region as shown in Fig. 3a. In the short-circuit case, a photocurrent $I_{\text{ph}} = V_{\text{OC}}/R_{\text{g}}$ is generated in the external circuit, where R_{g} is the graphene resistance as shown by Fig. 3b. Unlike in conventional Schottky barrier metal-semiconductor-metal (MSM) photodetectors, in which a high bias larger than that in the flat-band condition is needed for high-bandwidth operation²⁹, the gapless (or very small gap) nature in single or few-layer graphene allows for the almost unimpeded transmission of carriers through the potential barriers shown in the right side

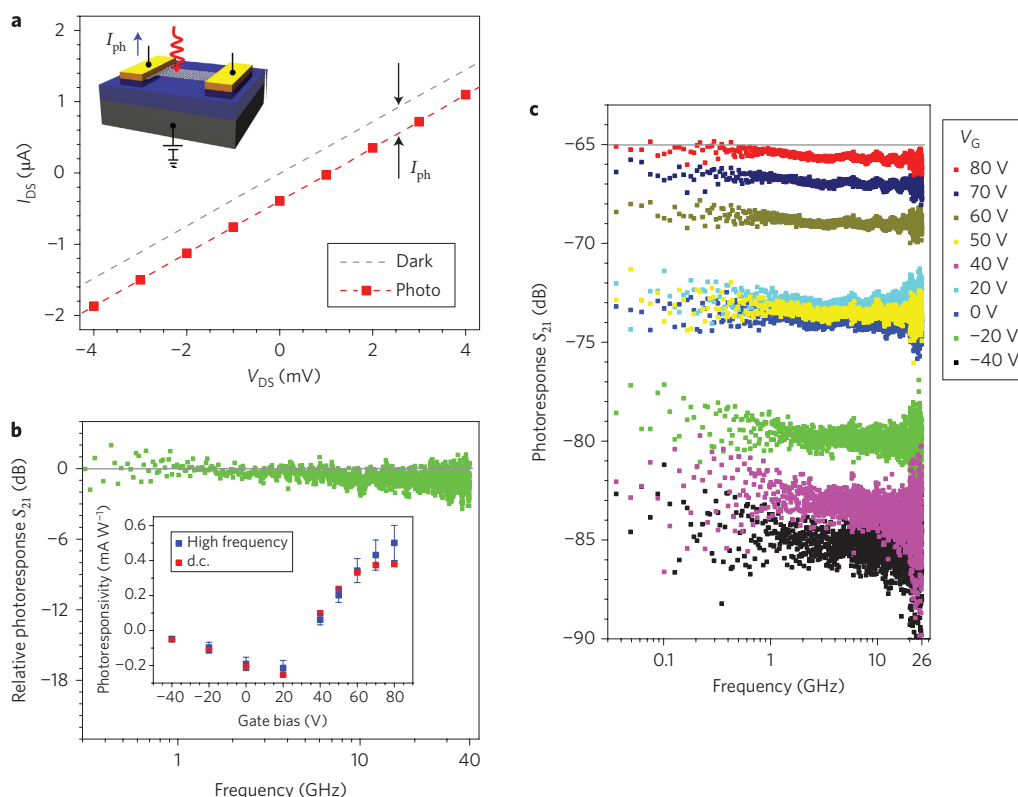


Figure 2 | Optical characterizations of the graphene photodetector. **a**, Typical I - V curves of the graphene photodetector without and with light excitation. Inset: schematic of the photocurrent measurement. The curved arrow in the inset represents the incident photon. **b**, Relative a.c. photoresponse $S_{21}(f)$ as a function of light intensity modulation frequency up to 40 GHz at a gate bias of 80 V. $S_{21} = 20 \times \log_{10}(R_{a.c.} \text{ (amp/watt)}/1 \text{ (amp/watt)})$ (dB), where $R_{a.c.} = \Delta I_{ph}/\Delta P_{in}$ (amp/watt). The curve is displaced vertically, so the response starts from 0 dB. A response degradation of ~ 1 dB is observed at 40 GHz, which is not due to the graphene photoresponse but instead is caused by the microwave probes. Inset: peak d.c. and high-frequency (a.c.) photoresponsivity as a function of gate bias. **c**, Absolute a.c. photoresponse $S_{21}(f)$ as a function of light intensity modulation frequency up to 26 GHz with gate bias (V_G) varying from -40 to 80 V. Here, S_{21} and $R_{a.c.}$ are defined as in Fig. 2b. However, absolute values are presented here. The response degradation of ~ 0.5 dB at 26 GHz is not caused by the graphene device, as in Fig. 2b. The a.c. photoresponsivity obtained here is presented in the inset of Fig. 2b.

of Fig. 3b, leading to high-bandwidth photodetection even at zero source-drain bias.

To generate a photocurrent in an external circuit, the photogenerated carriers must exit the photogeneration region before they recombine. If we assume that the carrier, under a strong E -field, can travel at a saturation velocity of $5.5 \times 10^5 \text{ m s}^{-1}$ at low carrier density³⁰, it would take only ~ 0.36 ps for the carriers to travel out of the ~ 200 -nm current generation region. Hence, the photogenerated carriers have a good chance of exiting the photogeneration region, resulting in reasonably good internal efficiency (6–16%) within the high E -field photodetection region, although the lifetime is short (tens of picoseconds) compared to those in conventional semiconductors. Although this short photocarrier lifetime in graphene is unfavourable for efficient photocurrent generation, it is desirable for other photonic applications such as optical switches, in which quick annihilation of photogenerated carriers is essential for high-speed operation.

The transit time limited bandwidth of the photodetector is given by²⁰

$$f_t = 3.5/2\pi t_{tr} \quad (2)$$

where t_{tr} is the transit time through the photodetection region. Thus, a value of f_t of 1.5 THz is obtained. If 200-nm-thick $\text{In}_{0.53}\text{Ga}_{0.47}\text{As}$ is used as the photodetection layer, the transit time limited bandwidth is around 150 GHz, which is ~ 10 times smaller than that in graphene²⁰ and mainly limited by the saturation velocity of the holes.

According to the I - V curve shown in Fig. 2a, the graphene photodetector and the high-frequency testing circuits can be simulated using the model shown in Fig. 3c. Compared to a conventional photodetector model in which the photodetector is reverse biased and modelled as an ideal current source^{20,21}, here the graphene photodetector can be modelled using either a current source or a voltage source with an internal resistance R_g . In the high-frequency S_{21} measurement, the photocurrent signal is transmitted through a 50Ω transmission line and finally to a matched load R_L of 50Ω . Here, the total capacitance $C_p + C_g$ ranges from 27 to 35 fF when the gate bias is in the range 30–80 V. According to this model, the calculated RC limited 3-dB bandwidth, $1/(2\pi R_L(C_g + C_p))$ is 106 GHz, assuming a total capacitance $C_g + C_p$ of 30 fF. Note that this is not the intrinsic limit of the current graphene photodetector, but a limit formed mainly by the pad capacitance. Measurements of similar, naked G-S pads in the gate bias range of 30–80 V yield a pad capacitance of 20 to 25 fF, implying that the C_g of this area of graphene ($\sim 3 \mu\text{m}^2$) should be 5–10 fF. If we assume a graphene capacitance of 5 fF, the RC limited bandwidth will be $1/(2\pi R_L C_g)$, which is ~ 640 GHz. Therefore, such graphene photodetectors will be limited mainly by RC because the transit time limited bandwidth is much larger (1.5 THz).

In summary, we have demonstrated ultrahigh-bandwidth photodetectors using single and few layer graphenes. In these novel photodetectors, the interaction of photons and graphene, the properties of the photogenerated carriers, and the transport of the photocarriers are fundamentally different from those in conventional group IV and III-V materials. These unique properties of graphene enable very

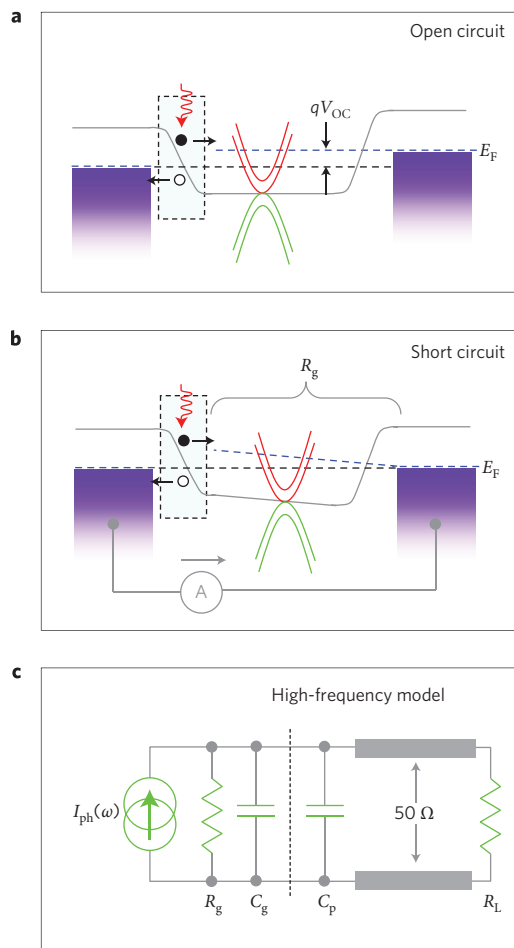


Figure 3 | Graphene photodetector circuit model and analysis. **a**, Potential profile and open-circuit voltage generation mechanism in a graphene photodetector operated under open-circuit conditions (V_{OC} , open-circuit voltage). **b**, Potential profile and photocurrent generation mechanism in a graphene photodetector operated under short-circuit conditions. Because photogeneration region is much smaller than the total graphene channel length (0.2 versus 1.2 μm), the resistance within the photogeneration region is ignored, and channel resistance R_g is used to represent the resistance of the rest of the channel. In both **a** and **b**, the curved red arrow denotes the incident photon, the black filled and open circles represent the photogenerated electron and hole, respectively, the solid grey line denotes the potential within the graphene channel, the dashed blue line shows the Fermi level (E_F), the dashed black line is a fiducial line to show the Fermi level variation across the channel, the violet rectangular boxes denote the metal contact, and the green and red parabolic curves represent a bilayer graphene band structure. **c**, High-frequency equivalent circuit model of the graphene photodetector. Components to the left of the dashed line (I_{ph} , R_g and C_g) represent the graphene device, and those to the right denote pad capacitance (C_p), $50\ \Omega$ transmission line and $50\ \Omega$ load. In the d.c. photocurrent measurement, $R_L = 0\ \Omega$ and short-circuit photocurrent is measured. In the high-frequency case, R_L ($50\ \Omega$) is still much smaller than the internal resistance R_g , so the detector still operates close to the short-circuit condition.

high bandwidth (potentially $>500\ \text{GHz}$) light detection, very wide wavelength detection range, zero dark current operation, good internal quantum efficiency and ease of fabrication.

Methods

Fabrication of the graphene photodetectors. The graphene photodetectors used in this study were prepared by ‘mechanical exfoliation’ of graphite and are similar to standard back-gated graphene transistors^{41,6,17}. Graphitic flakes were deposited on

the surface of a silicon substrate covered by 300-nm-thick silicon dioxide and pre-patterned alignment marks. To reduce the parasitic capacitance, a highly resistive wafer (1–10 k $\Omega\ \text{cm}$) was used. Single- and few-layer graphenes were identified by visual inspection with an optical microscope and their number was further confirmed by Raman spectroscopy²⁵. Electron-beam lithography was used to pattern the signal and ground contact electrodes, and metal films (Ti/Pd/Au, 0.5/20/20 nm) were deposited using electron-beam evaporation. The electrical contact pads were designed as $50\ \Omega$ coplanar transmission lines for on-wafer high-speed characterization. These had dimensions of $80 \times 80\ \mu\text{m}^2$ and were separated by $40\ \mu\text{m}$. Devices with two types of wirings were fabricated: ground–signal (G–S) and ground–signal–ground (G–S–G) (see Fig. 1a). The graphene channels were 1 or 2 to 3 layers thick, 1–2 μm long and 1–2.5 μm wide. In the G–S–G configuration, the signal electrode had a width of $\sim 150\ \text{nm}$ as shown in Fig. 1a. The results reported in this study were obtained from devices with G–S wirings. Overnight annealing of the as-prepared samples in an ultrahigh-vacuum chamber at 400 K was performed before measurements in ambient conditions. When sweeping the back-gate bias, we typically observed maximum device resistance (‘Dirac point’) at 20 to 40 V.

High-frequency electrical characterization of the photodetectors. The electrical characteristics of the photodetectors were inferred from on-chip radio-frequency measurements up to 20 GHz using an Agilent E8364C parameter network analyser. A standard short–open–load (SOL) calibration substrate (from GGB Industries) was used for calibrating the frequency-dependent response in the network analyser, the 3.5-mm cabling, and the microwave probe (GGB Industries) to ensure accurate on-wafer testing. The complex-valued, high-frequency device impedance Z_{IN} was determined by measuring the frequency-dependent reflection coefficient Γ_{IN} (S_{11} scattering parameter) and calculating Z according to $Z_{IN} = Z_0(1 + \Gamma_{IN})/(1 - \Gamma_{IN})$, where Z_0 is the $50\ \Omega$ system impedance. The lumped circuit model of the photodetector was extracted based on measurement and subsequent fitting of the model parameters. The gate bias (up to 80 V) was applied using a HP 4145C semiconductor parameter analyser.

High-frequency optical characterization of the photodetectors. Optical photodetector characterization was performed using two different sets of Agilent Lightwave Component Analyzers (LCA), N4375B and N4373C, each with a built-in 1,550 nm laser. The highest light intensity modulation frequencies available in N4375B and N4373C are 26 GHz and 67 GHz, respectively. Other microwave components in our setup including cables and probes were limited to 40 GHz. The relative photoresponse in Fig. 2b was measured using the N4373C, because it provides a higher modulation frequency. The absolute photoresponses at various gate biases shown in Fig. 2c were measured using the N4375B, because it has lower noise floor and therefore allows for the measurement of small photoresponse signals. Frequency response characterization was achieved by sweeping the light modulation frequency. The optical fibre output of the LCA ($-2\ \text{dB m}$) was amplified using an erbium-doped fibre amplifier (EDFA). The EDFA output was then coupled into free space and focused to a diffraction limited spot ($\sim 2\ \mu\text{m}$, full-width at half-maximum diameter) on the device using a $\times 20$ magnification, long-working-distance microscope objective. A piezoelectrically driven mirror, mounted before the objective, allowed us to position the beam on the sample with nanometre spatial precision. The total incident optical power on the sample was 3 mW (4.8 dBm). The photocurrent signal was extracted through a G–S microwave probe (GGB Industries) and was fed back into the input port of the parameter network analyser. The frequency-dependent S_{21} scattering parameter, which is defined as $S_{21} = 20 \times \log_{10}(R_{a.c.} / 1\ \text{amp/watt}) / 1\ \text{amp/watt}$ (dB), was recorded as the modulation frequency was swept between 10 MHz and 26 GHz. From this measurement, the high-frequency a.c. responsivity $R_{a.c.} = \Delta I_{ph} / \Delta P_{in}$ was then determined. The impact of the EDFA on the responsivity was calibrated out in the final data. The gate bias was applied using a HP 4145C semiconductor parameter analyser.

Received 16 June 2009; accepted 24 August 2009;
published online 11 October 2009

References

- Novoselov, K. S. *et al.* Electric field effect in atomically thin carbon films. *Science* **306**, 666–669 (2004).
- Novoselov, K. S. *et al.* Two-dimensional gas of massless Dirac fermions in graphene. *Nature* **438**, 197–200 (2005).
- Zhang, Y., Tan, J. W., Stormer, H. L. & Kim, P. Experimental observation of the quantum Hall effect and Berry’s phase in graphene. *Nature* **438**, 201–204 (2005).
- Avouris, Ph., Chen, Z. & Perebeinos, V. Carbon-based electronics. *Nature Nanotech.* **2**, 605–615 (2007).
- Geim, A. K. & Novoselov, K. S. The rise of graphene. *Nature Mater.* **6**, 183–191 (2007).
- Lin, Y. M. *et al.* Operation of graphene transistors at gigahertz frequencies. *Nano Lett.* **9**, 422–426 (2009).
- Nair, R. R. *et al.* Fine structure constant defines visual transparency of graphene. *Science* **320**, 1308 (2008).

8. Wang, F. *et al.* Gate-variable optical transition in graphene. *Science* **320**, 206–209 (2008).
9. Chuang, S. *Physics of Optoelectronic Devices* (Wiley, 1995).
10. Li, Z. Q. *et al.* Dirac charge dynamics in graphene by infrared spectroscopy. *Nature Phys.* **4**, 532–535 (2008).
11. Ryzhii, V., Mitin, V., Ryzhii, M., Ryabova, N. & Otsuji, T. Device model for graphene nanoribbon phototransistor. *Appl. Phys. Exp.* **1**, 063002 (2008).
12. Vasko, F. T. & Ryzhii, V. Voltage and temperature dependencies of conductivity in gated graphene. *Phys. Rev. B* **76**, 233404 (2007).
13. George, P. A. *et al.* Ultrafast optical-pump terahertz-probe spectroscopy of the carrier relaxation and recombination dynamics in epitaxial graphene. *Nano Lett.* **8**, 4248–4251 (2008).
14. Rana, F. *et al.* Carrier recombination and generation rates for intravalley and intervalley phonon scattering in graphene. *Phys. Rev. B* **79**, 115447 (2009).
15. Lee, E. J. H., Balasubramanian, K., Weitz, R. T., Burghard, M. & Kern, K. Contact and edge effects in graphene devices. *Nature Nanotech.* **3**, 486–490 (2008).
16. Xia, F. *et al.* Photocurrent imaging and efficient photon detection in a graphene transistor. *Nano Lett.* **9**, 1039–1044 (2009).
17. Mueller, T., Xia, F., Freitag, M., Tsang, J. & Avouris, Ph. Role of contacts in graphene transistors: a scanning photocurrent study. *Phys. Rev. B* **79**, 245430 (2009).
18. Ishibashi, T. *et al.* InP/InGaAs uni-travelling-carrier photodiodes. *IEICE Trans. Electron.* **E83-C**, 938–949 (2000).
19. Ito, H., Furuta, T., Kodama, S. & Ishibashi, T. InP/InGaAs uni-travelling-carrier photodiodes with a 340 GHz bandwidth. *Electron. Lett.* **36**, 1809–1810 (2000).
20. Kato, K., Kawano, K. & Kozen, A. Design of ultra-wide band, high sensitivity p–i–n photodetectors. *IEICE Trans. Electron.* **E76-C**, 214–221 (1993).
21. Xia, F. *et al.* An asymmetric twin-waveguide high-bandwidth photodiode using a lateral taper coupler. *IEEE Photon. Technol. Lett.* **13**, 845–847 (2001).
22. Gmachl, C. *et al.* New frontiers in quantum cascade lasers and applications. *IEEE J. Sel. Top. Quantum Electron.* **6**, 931–947 (2000).
23. Mittleman, D. M., Jacobsen, R. H. & Nuss, M. C. T-ray imaging. *IEEE J. Sel. Top. Quantum Electron.* **3**, 679–692 (1996).
24. Wang, J., Gudiksen, M. S., Duan, X., Cui, Y. & Lieber, C. M. Highly polarized photoluminescence and photodetection from single indium phosphide nanowires. *Science* **293**, 1455–1457 (2001).
25. Ferrari, A. C. *et al.* Raman spectrum of graphene and graphene layers. *Phys. Rev. Lett.* **97**, 187401 (2006).
26. Wolff, I. *Coplanar Microwave Integrated Circuits* Ch.1 (Wiley, 2006).
27. Demiguel, S. Analysis of partially depleted absorber waveguide photodiodes. *IEEE J. Lightwave Technol.* **23**, 2505–2512 (2005).
28. Guo, J., Yoon, Y. & Ouyang, Y. Gate electrostatics and quantum capacitance of graphene nanoribbons. *Nano Lett.* **7**, 1935–1940 (2007).
29. Sze, S. M., Coleman, D. J. & Loya, A. Current transport in metal–semiconductor–metal (MSM) structures. *Solid-State Electron.* **14**, 1209–1218 (1971).
30. Meric, I. *et al.* Current saturation in zero-bandgap, top-gated graphene field-effect transistors. *Nature Nanotech.* **3**, 654–659 (2008).

Acknowledgements

The authors are grateful to M. Freitag and Z. Chen for helpful discussions, to Y. Vlasov, S. Assefa, W. Green, C. Schow and L. Schares for help with the radio-frequency measurements, to J. Tsang for Raman measurements, and to B. Ek and J. Bucchignano for technical assistance. F.X. is indebted to C.Y. Sung for his encouragement. T.M. acknowledges financial support by the Austrian Science Fund FWF (Erwin Schrödinger fellowship J2705-N16).

Additional information

Supplementary information accompanies this paper at www.nature.com/naturenanotechnology. Reprints and permission information is available online at <http://npg.nature.com/reprintsandpermissions/>. Correspondence and requests for materials should be addressed to F.X. and P.A.